Equilibrium theory of cylindrical discharges with special application to helicons

Davide Curreli[a)] and Francis F. Chen[b)]

Electrical Engineering Department, University of California, Los Angeles, California 90095-1594, USA

Radiofrequency discharges used in industry often have centrally peaked plasma density profiles $n(r)$ although ionization is localized at the edge, even in the presence of a dc magnetic field. This can be explained with a simple cylindrical model in one dimension as long as the short-circuit effect at the endplates causes a Maxwellian electron distribution. Surprisingly, a universal profile can be obtained, which is self-similar for all discharges with uniform electron temperature T_e and neutral density n_n. When all collisions and ionizations are radially accounted for, the ion drift velocity toward the wall reaches the Bohm velocity at a radius which can be identified with the sheath edge, thus obviating a pre-sheath calculation. For non-uniform T_e and n_n, the profiles change slightly but are always peaked on axis. For helicon discharges, iteration with the HELIC code for antenna-wave coupling yields profiles consistent with both energy deposition and diffusion profiles. Calculated density is in absolute-value agreement with experiment. © *2011 American Institute of Physics*. [doi:10.1063/1.3656941]

I. INTRODUCTION

Studies of gas discharges began with the work of such pioneers as Thomson[1] and Irving Langmuir.[2] Later, Chapman and Cowling[3] worked out a detailed mathematical theory on local properties such as distribution functions, diffusion, viscosity, and thermal conduction in partially ionized plasmas. Biberman *et al.*[4] added ionization, recombination, and radiative transport. The book by Delcroix[5] covers these local properties, including cross sections, and goes on to the macroscopic behavior of discharge plasmas, including ambipolar diffusion. Delcroix's next book[6] repeats the general principles of collisions and transport but goes on to define an "intermediate regime" in which electrons are Maxwellian but ions are not. This is a precursor to the "presheath." Up to this point, the research, except for Langmuir's, was purely mathematical, with no consideration of actual experiments, of which there were few at that time. Franklin's book[7] was finally written from an experimental viewpoint, with reference to the positive column and its behavior under magnetic fields and time variation. He considered the conditions at the wall, where the plasma density should be finite instead of zero, and concluded that there must be both a sheath and a presheath. In these early years, there were no treatments of an entire discharge, giving, for instance, its density profile and its boundary conditions at the walls. However, the scene had been set by the solutions for collisionless plasmas confined between the infinite plane plates.[8,9] Whether the ionization is uniform or proportional to the electron density, an analytical solution can be obtained for the plasma potential ϕ as a function of the distance from the midplane. This "plasma solution" for the quasineutral region developed an infinite slope at the famous point, where $e\phi/KT_e = -0.854$,

and then became double-valued. That was obviously, where the solution had to be stopped and matched to the Debye sheath, a much thinner region which is not quasineutral.

The sheath boundary conditions of plasma, particularly as applied to the surface of a probe, have been studied extensively. The function of the Debye sheath is to form a potential barrier to repel electrons so that they will escape to the wall no faster than the ions. Thus, the wall has to be negatively relative to the plasma, and the potential in the sheath has to curve downwards from its edge to the wall. It was shown by Bohm[10] and explained by Chen[11] that this requires the ions to enter the sheath with a drift velocity at least as large as the acoustic velocity. This is known as the Bohm criterion. It requires a mechanism for accelerating the ions in the quasineutral region and turning their distribution into a mono-directional one. This is the electric field in a presheath, a region much thicker than the Debye sheath but usually thinner than the plasma radius. A review article by Riemann[12] explains sheaths and presheaths in great detail. Both ionization and collisions permit the buildup of an electric field in the presheath, which, therefore, has the scale of the collision and ionization scale lengths. In the spirit of boundary layer analysis, the plasma, presheath, and sheath are assumed to have greatly differing scale lengths, and they are matched to one another at points which have been subject to great debate. The theory presented here avoids this problem by a more exact treatment.

The science of partially ionized plasmas advanced rapidly with the rise of the computer age, since plasmas are needed for the etching and plasma enhanced chemical vapor deposition of semiconductor chips. Most plasma tools are powered by radiofrequency (rf) generators. Capacitively coupled plasmas (CCPs) are planar and are outside the purview of this paper, which assumes cylindrical symmetry. Inductively coupled plasmas (ICPs), usually cylindrical, may or may not have a dc magnetic field (B-field). Descriptions

---

a)Electronic mail: davide.curreli@unipd.it.
b)Electronic mail: ffchen@ee.ucla.edu.

of these plasma sources can be found in textbooks.[13,14] Among ICPs with a B-field, the most interesting is the helicon discharge. Helicon discharges are known to produce high plasma densities for such purposes as plasma processing and spacecraft propulsion. These plasma sources are unique because they depend on the physical properties of plasma waves, particularly, the helicon wave, which is the "whistler" wave of space physics but confined inside a cylinder. It is now believed that the helicon wave mode-couples at the boundary to an electron cyclotron wave, called the Trivelpiece-Gould (TG) mode;[15] and it is the TG wave that absorbs the rf energy efficiently. The reason is that the TG mode has a slow group velocity radially inwards, losing its energy to electrons by collisional absorption and by nonlinear processes.[16] Several computer codes, to be named later, have been devised to calculate the wave and absorption properties of coupled helicon-TG waves. However, these codes do not treat the equilibrium state of the entire discharge. In this paper, we write a code EQM to describe a discharge in general and then iterate it with a helicon code to apply it specifically to helicon discharges.

Our motivation comes from the experimental data that contradict the theories described above. For instance, in the case of an ICP with no B-field, we have observed anomalous skin effect. Figure 1 shows an ICP with an antenna wound around the circumference. In Fig. 2, it is seen that the classical skin depth of 3 cm is such that very little rf power can reach the axis. Nonetheless, the plasma density is peaked on axis, although the electron temperature KT_e does show a peak near the antenna. In the case of a helicon discharge with a strong B-field, it is known that the TG mode will deposit most of the rf energy near the boundary. Nonetheless, almost all helicon data have shown density peaks on axis, as illustrated by the early data of Fig. 3 by Boswell.[17] To explain such data in the spirit of interaction between theory and experiment, we have tried to make a simple model which neglects effects that are too small to be distinguishable in
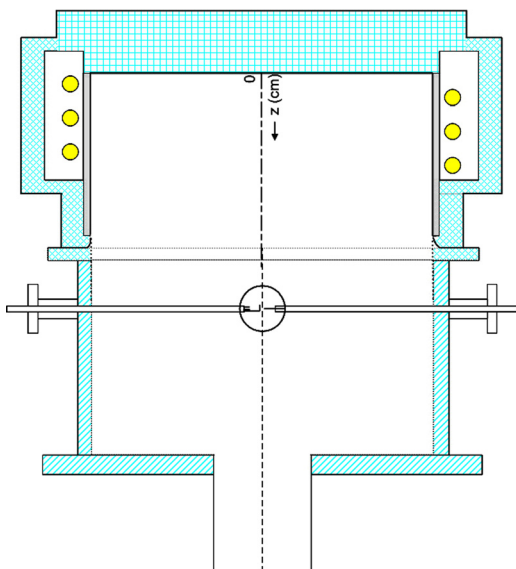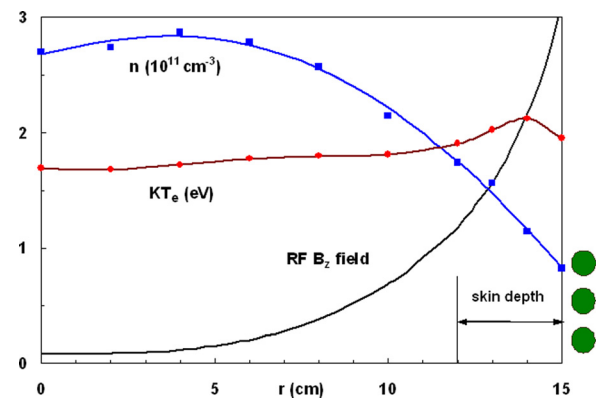

FIG. 2. (Color online) Radial profiles of plasma density, electron temperature, and RF field in the machine in Fig. 1. Data were taken by J. D. Evans in our laboratory in 1998 under contract with PlasmaTherm.

experiment but retains the essential elements of most actual experiments.

In the modern era, the equilibrium state of low-pressure gas discharges has been studied by Godyak,[18] Lieberman and Lichtenberg,[19] Sternberg *et al.*,[20] and Fruchtman *et al.*[21,22] The latter two papers tackled the equilibrium problem of rf discharges with dc B-fields starting with essentially the same governing equations that we use here. However, these very long papers cover the general case in great mathematical detail and do not use the short-circuit effect that is

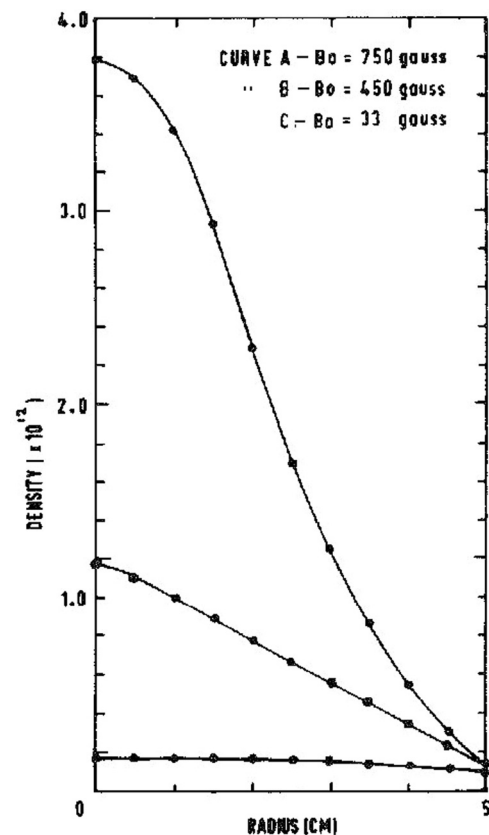FIG. 1. (Color online) An ICP by PlasmaTherm® with m = 0 antenna on the circumference of the chamber.

FIG. 3. Radial density profiles at three B-fields in a 10-cm diameter helicon discharge in 1.5 mTorr of argon, driven by 600 W of rf at 8 MHz. Reprinted with permission from Boswell, Phys. Lett. A **33**, 457 (1970). Copyright © 1970, Elsevier Press.

essential to this paper. Without that effect, they could not explain the universality of centrally peaked density profiles. Our approach yielded a surprising result: the equilibrium profiles of all discharges of normal length have similar shapes, independent of magnetic field. Thus, our result applies not only to helicon discharges but also to discharges without B-fields, including those of the pioneers named above.

II. BASIC EQUATIONS AND ASSUMPTIONS

We consider a plasma in an infinite circular cylinder of radius a in which all quantities depend only on the coordinate r. There is a uniform, coaxial magnetic field $B\hat{z}$. We can neglect the effect of **B** on the ions for the following reason. Ions are accelerated by electric fields which are generated by electrons and are scaled to their temperatures. If KT_e is of order 3 eV and B of order 100G, the ion Larmor diameter of a 2-eV argon ion, say, is $\approx$26 cm, and few ions can make a complete orbit within the discharge. Their orbits may be curved, but ion motion in the θ direction cannot change the ions' radial positions. Also, the ions cannot gain energy from a dc magnetic field because the Lorentz force is perpendicular to their velocity. Hence, the ions can be considered unmagnetized. At much larger B-fields, the ion orbits may be smaller than a, but radial electric fields E_r can only cause the ions to drift in the ignorable direction θ. There are no azimuthal E-fields in steady state, there being no dc current in the z direction. Hence, we can ignore the effect of **B** on ion motions even at 1000G. Radial ion motion is controlled by E_r and charge-exchange collisions with neutrals. At 3 eV, argon ions have a mean free path of order 14 cm at 1 mTorr and 0.7 cm at 20 mTorr, and therefore, neither the collisionless nor the highly collisional limit is applicable, and collisions have to be treated explicitly. The equation of motion describing the ion fluid in equilibrium is[21,23]

$$M\mathbf{v}\nabla \cdot (n\mathbf{v}) + Mn\mathbf{v} \cdot \nabla\mathbf{v} - en\mathbf{E} + Mn\nu_{io}\mathbf{v}$$
$$= en(\mathbf{v} \times \mathbf{B}) - KT_i\nabla n \approx 0. \qquad (1)$$

Here, M is the ion mass, n the quasineutral plasma density, $\mathbf{v}$ the ion fluid velocity, and ν_{io} the charge-exchange collision frequency, whose evaluation is given in the Appendix. The first term in Eq. (1) accounts for drag due to ionization, which injects slow ions into the fluid. The nonlinear $\mathbf{v} \cdot \nabla\mathbf{v}$ term converts Newton's law from a frame moving with the ions to one that is stationary in the laboratory frame. Its physical meaning is explained by Chen.[24] The two terms on the right-hand side will be neglected, the $\mathbf{v} \times \mathbf{B}$ term for the reason stated above, and the T_i term because T_i is usually $\ll T_e$. The ions will be accelerated by **E**, which scales with T_e.

It will be convenient to define the ionization and collision probabilities P_c and P_i as follows:

$$P_i(r) \equiv \langle\sigma v\rangle_{ion}(r), \quad P_c(r) \equiv \langle\sigma v\rangle_{cx}(r) = \nu_{io}/n_n, \qquad (2)$$

where n_n is the density of neutral atoms. The ion equation of continuity can then be written

$$\nabla \cdot (n\mathbf{v}) = nn_nP_i(r). \qquad (3)$$

Using Eqs. (2) and (3) in Eq. (1) and neglecting the right-hand side, we now have

$$M\mathbf{v} \cdot \nabla\mathbf{v} - e\mathbf{E} + Mn_n(P_i + P_c)\mathbf{v} = 0. \qquad (4)$$

We now neglect variations in ϕ and z, reducing the problem to one dimension in r, and suppress the subscript r so that $v \equiv v_r$. With the usual definitions

$$\mathbf{E} = -\nabla\phi, \quad \eta \equiv -e\phi/KT_e, \quad \text{and} \quad c_s \equiv (KT_e/M)^{1/2}, \qquad (5)$$

the radial component of Eq. (4) becomes

$$v\frac{dv}{dr} = c_s^2\frac{d\eta}{dr} - n_n(P_c + P_i)v. \qquad (6)$$

This is the ions' equation of motion. Their equation of continuity, Eq. (3), can be written as

$$\frac{dv}{dr} + v\frac{d(\ln n)}{dr} + \frac{v}{r} = n_nP_i(r). \qquad (7)$$

We next consider the electron fluid. Its equation of motion is

$$mn\mathbf{v} \cdot \nabla\mathbf{v} = -en(\mathbf{E} + \mathbf{v} \times \mathbf{B}) - KT_e\nabla n - mn\mathbf{v}(\nu_{eo} + \nu_{ei}), \qquad (8)$$

where the collision frequencies are with neutrals and ions. Since the electrons are magnetized, classical diffusion theory[13,25] would predict that their rate of diffusion across **B** would be slower than that of the unmagnetized ions. This would give rise to a plasma potential that is more negative at the center than at the edge. In experiment, the opposite is usually observed; the potential peaks at the center just as does the density, in rough agreement with Boltzmann's relation [Eq. (9)],

$$n = n_0e^{e\phi/KT_e} = n_0e^{-\eta}. \qquad (9)$$

The discrepancy can be resolved if the discharges are not infinitely long, and electrons can reach the ends of the chamber well before they can reach the periphery. In this case, the Simon short-circuit effect[26] must be taken into account. Though this effect has been known for a long time, its application to modern devices has not been well understood. The short-circuit effect will be fully discussed in Sec. V. For the time being, we explore the consequences of the validity of Eq. (9) throughout the whole plasma.

III. A "UNIVERSAL" DENSITY PROFILE

The derivative of Eq. (9) is

$$\frac{d(\ln n)}{dr} = -\frac{d\eta}{dr}. \qquad (10)$$

Inserting this into Eq. (7) gives

$$\frac{dv}{dr} - v\frac{d\eta}{dr} + \frac{v}{r} = n_nP_i(r). \qquad (11)$$

Equation (6) can be written as

$$\frac{d\eta}{dr} = \left[v\frac{dv}{dr} + n_n(P_i + P_c)v \right] c_s^{-2}. \qquad (12)$$

Finally, substituting this into Eq. (11) yields an ordinary differential equation (ODE) for v,

$$\frac{dv}{dr} + \frac{v}{r} - \frac{v^2}{c_s^2}\left[\frac{dv}{dr} + n_n(P_i + P_c)\right] = n_n P_i(r) \qquad (13)$$

or

$$\frac{dv}{dr} = \frac{c_s^2}{c_s^2 - v^2}\left[-\frac{v}{r} + n_n P_i(r) + \frac{v^2}{c_s^2} n_n(P_i + P_c)\right]. \qquad (14)$$

The "plasma solution" given by this equation clearly diverges when $v \to c_s$. The Bohm criterion for sheath formation[12] is satisfied at the radius r_a where this occurs, and that radius can be identified as the discharge tube radius a if the sheath thickness is negligible. The value of r_a apparently depends on the physical quantities n_n, c_s, P_c, and P_i, but it will turn out that the dependence is very weak. Normalizing v to c_s by

$$u \equiv v/c_s, \qquad (15)$$

we can write Eq. (14) as

$$\frac{du}{dr} = \frac{1}{1-u^2}\left\{ -\frac{u}{r} + \frac{n_n}{c_s}P_i(r)\left[1 + u^2(1 + P_c/P_i)\right]\right\}. \qquad (16)$$

For clarity, we now define

$$k(r) \equiv 1 + P_c(r)/P_i(r), \qquad (17)$$

so that Eq. (16) becomes

$$\frac{du}{dr} = \frac{1}{1-u^2}\left[-\frac{u}{r} + \frac{n_n}{c_s}P_i(1 + ku^2)\right]. \qquad (18)$$

Since $n_n P_i/c_s$ has dimensions of (length)$^{-1}$, we can now introduce a dimensionless independent variable ρ defined by

$$\rho \equiv (n_n P_i/c_s)r, \qquad (19)$$

obtaining

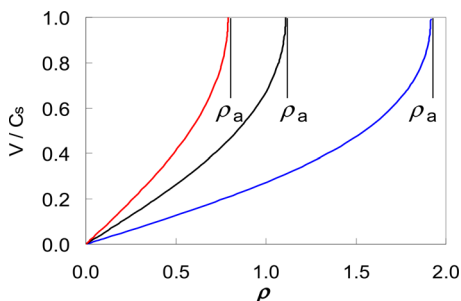$$\frac{du}{d\rho} = \frac{1}{1-u^2}\left[1 + ku^2 - \frac{u}{\rho}\right]. \qquad (20)$$

FIG. 4. (Color online) Solutions of Eq. (20) for three different values of k. In each case, the sheath edge ρ_a occurs at a different value of ρ.
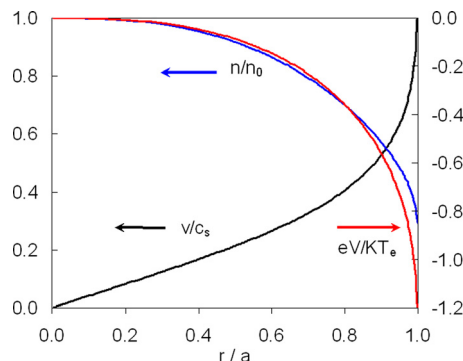

FIG. 5. (Color online) Rescaled solution of Eq. (20) for 15 mTorr of argon and $KT_e = 3$ eV, yielding v/c_s, n/n_0 (upper curve), and eV/KT_e (lower curve, right scale). The latter two are related by the Boltzmann relation. The abscissa is normalized so that the sheath edge occurs at $r = a$. The curve retains the same shape for any value of a.

In these units, the solution for u, which will also yield the density and potential profiles, depends only on the parameter k in the nonlinear term. Let us first see what the profiles look like when $k(r)$ is constant.

IV. SOLUTIONS FOR CONSTANT n_n AND KT_e

In this case, k is independent of r. Equation (20) is a nonlinear ODE which can be solved numerically. Using a variable-step Runge-Kutta method, we obtain a unique solution for each k, starting with $u = 0$ at $\rho \cong 0$. Three such solutions are shown in Fig. 4, each with a radius ρ_a where $v = c_s$. Since the sheath edge must be located at this point, the curves can be renormalized to fit a discharge tube of radius a by setting r/a equal to ρ/ρ_a. From the solution for $v(r)$, Eqs. (12) and (10) can be used to find $\eta(r)$ and $n(r)/n_0$, respectively. After a rescaling of Fig. 4, Fig. 5 shows the radial profiles of v/c_s, n/n_0, and $-\eta(r)$ for one k-value corresponding to particular values of KT_e and neutral pressure p_0.

The nature of Eq. (20) is revealed when the parameters n_n, c_s, or P_i in Eq. (19) are varied. The values of ρ_a change when k changes, but n_n and c_s do not appear in k, so the curves in Fig. 5 are unaffected by a change in n_n, for instance. This is shown in Fig. 6. The profiles for three different pressures are identical when plotted against r/a. The
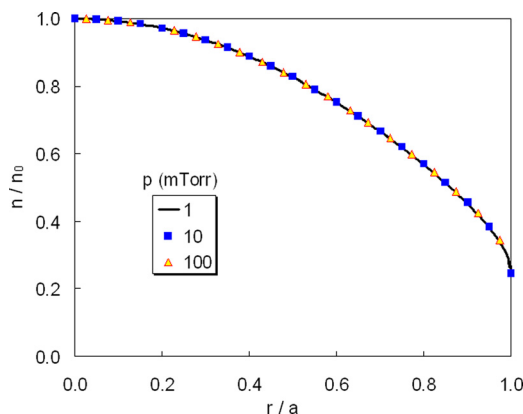

FIG. 6. (Color online) Universal density curves for $KT_e = 3$ eV argon discharges at various pressures.

solutions of Eq. (20) depend only on the ratio of P_c to P_i. The curves like those of Fig. 5 are "universal" in the sense that they are independent of the values of a, n_n, and n_0. These renormalized curves change only when the nonlinear term ku^2 changes. In Fig. 7, P_c is fixed but T_e is changed, greatly altering the ionization term P_i and hence k.

Note that our basic assumptions have removed the magnetic field from the equations. Hence, the results up to now apply to all low-pressure discharges of reasonable length with or without dc B-fields. Although solutions of Eq. (20) have recovered the centrally peaked density profiles usually observed, such as those in Figs. 2 and 3, they cannot be seriously compared with experiment because, for instance, the values of n_n and KT_e cannot be chosen independently, their radial variations have not been taken into account, and the z-dependences have been neglected. The ion fluid equation used here gives a single, averaged value of v at each radius when, in fact, the ions have a distribution depending on where they were created. We have included the ionization-drag term to account for this roughly. Intricate kinetic-theory calculations of the ion distribution function, as done by our pioneers,[3,5] have masked the essential physics. In addition, detailed comparison with experiment requires treatment of ionization balance, neutral depletion, and energy balance. Except for z variations, these effects are the subjects of subsequent sections. The papers by Sternberg et al.[20] and Fruchtman et al.[21,22] use the same ion fluid equations but do not assume the Boltzmann relation. In covering a wider range of parameters and dimensions, those efforts required such extensive algebra that physical insights were not obvious. Their results differ from ours because diffusion across magnetic fields was assumed to be classical instead of being controlled by the short-circuit effect.

The independence of pressure in Fig. 6 has not been seen by other authors. For instance, Lieberman and Lichtenberg,[19] while using the Boltzmann relation, quote a result by Godyak[27] that the center-to-edge density ratio should vary approximately with $n_n^{1/2}$. This was the result of numerous approximations needed to obtain analytic formulas. Furthermore, the ion *fluid* equation was not used, so the nonlinear ku^2 term in Eq. (20), which contains the plasma parameters, was not obtained at all. Our results that the profiles do not depend on n_n and a are caused by a physical cancellation
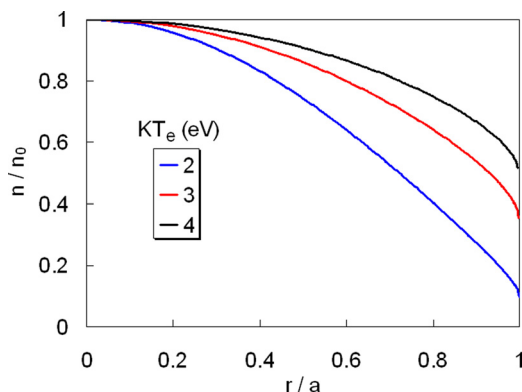

FIG. 7. (Color online) Density curves for 15-mTorr argon discharges at various KT_e for fixed n_n. The curves are reversed from the order in the legend.

that could not have been found with algebraic approximations. In our work, the presheath is treated as a part of the plasma, and the plasma solution is matched to the Debye sheath not at a particular value of the potential η, but at a particular value of the ion velocity. As a consequence, if the neutral density is changed, it takes the same number of collisions for the ion velocity to reach c_s, and the density profile is unchanged. For example, for the conditions of intermediate collisionality that we are considering, if n_n is decreased, the mean free path is longer and dn/dr is smaller. The Boltzmann relation then predicts a lower E_r. The ions accelerate more slowly and travel farther to reach c_s. But the *changes* in v and E_r depend on collisions, and the same profile of v is obtained when plotted against r/a. This is not exact, but it does give insight into the physics.

The profile of $T_e(r)$, and hence of $P_i(r)$, cannot be calculated until the energy balance is calculated in Sec. IX, but $P_c(r)$ can be evaluated accurately because the solution of Eq. (20) gives $v(r)$ at each radius. Thus, the collision frequency ν_{io} is *not* $n_n\langle\sigma v\rangle_{cx}$ averaged over a Maxwellian ion distribution at a temperature T_i as given by Eq. (2), but is fixed by the known velocity at each radius,

$$\nu_{io} = n_n\sigma_{cx}(E_i)v(r), \qquad (21)$$

where $v(r)$ is given by the curve in Fig. 5, and the ion energy is $E_i = \frac{1}{2}Mv^2$. The charge-exchange cross section as a function of E_i is given in the Appendix. Since the ions are accelerated radially by the electric field E_r, which scales with T_e, $E_i(r)$ and ν_{io} are the functions of T_e and not T_i except in a vanishingly small region near the axis. It is a much weaker function of T_e than ν_{ion}, so the "universal" profiles of Fig. 5 will not be greatly changed by this exact evaluation of $P_c(r)$. With use of Eq. (21) for $n_nP_c(r)$, the ratio $P_c(r)/P_i(r)$ depends only on T_e, and the function $k(r) = P_c(r)/P_i(r)$ will vary in a predictable way as $v(r)$ changes, taking into account the variation of ν_{io} as the ions are accelerated radially. Though small, this variation of $P_c(r)$ can easily be included in future computations, including those in which n_n and T_e are not constant.

To summarize this section: (a) That such "universal" radial profiles, valid for any pressure or discharge diameter, can be obtained, is a direct consequence of the use of the short-circuit effect to make the electron Boltzmann relation valid across the magnetic field. (b) Since the magnetic field did not enter into the calculations so far, these results are valid for any cylindrical discharge when end losses can be neglected. (c) Equation (20) naturally defines the sheath edge since $du/d\rho \to \infty$ when $u = 1$, $v = c_s$. Assumption of a pre-sheath is not needed since all collisions and ionizations are evaluated locally at every radius up to the sheath edge.

V. THE SHORT-CIRCUIT EFFECT

One end of a finite-length discharge in a magnetic field is shown in Fig. 8. Electrons are strongly magnetized, so they bounce back and forth between endplates, traversing the length in nanoseconds. Their diffusion to the sidewall is slow, and they are lost mainly to the endplates. Ions, on the
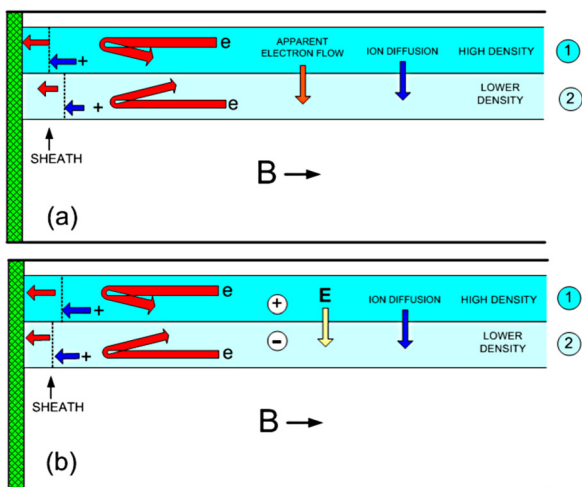
FIG. 8. (Color online) Sheath configuration (a) during the short-circuit effect and (b) during the approach to equilibrium.

other hand, are not magnetized, so they diffuse both radially to the sidewall and axially to the endplates. To keep the plasma quasineutral, the much more mobile electrons must reach the endplates with a flux equal to the ion flux. This is accomplished by Debye sheaths at the endplates that form Coulomb barriers allowing only a small portion of the electron flux to leak through to the endplate.

Specifically, the ion flux at the sheath edge is $n_s c_s$, and the electron flux is $n_s v_{the}$, where the electron thermal velocity in one direction is $\nu_{the} = \sqrt{(KT_e/2\pi m)}$, and the density n_s at the sheath edge is $\approx 0.5n$. In each tube of magnetic lines, of which two are shown in Fig. 8, the electrons can move freely, so they are locally Maxwellian. So far, there is no communication between tubes, so the plasma potential ϕ_p relative to the endplate is arbitrary in each tube. The sheath reduces the electron flux by $\exp(-e\phi_p/KT_e)$. Equal fluxes then require

$$\frac{e\phi_p}{KT_e} = \ln\left(\frac{M}{2\pi m}\right)^{1/2}. \tag{22}$$

This is the well known condition for the floating potential of a probe and does not involve the density at all. The plasma is always positive relative to the endplate, but each tube can have an arbitrary density and potential, independent of its neighbors. This is, of course unreal, since tubes can communicate with one another through ion motions. The ions can move radially, and the short-circuit effect allows the electrons to follow them across **B** in the following way. Consider the two tubes labeled 1 and 2 in Fig. 8(a). Suppose ionization is higher near the wall than near the axis. Then tube 1 will have higher density, and the sheath drop will adjust itself so that the electron and ion fluxes to the endplate are equal. Initially, tube 2 will have lower density, with equal numbers of ions and electrons created, so the sheath drop is the same as in tube 1 and given by Eq. (22). However, ions diffusing inward due to their density gradient will upset this balance; there will be more ions than electrons in tube 2. The sheath drop in tube 2 must be larger than in tube 1 to confine more electrons and raise their density. This is represented pictori-

ally in Fig. 8(a) by a larger sheath thickness (greatly exaggerated). Though both fluxes are smaller in tube 2, the sheath thickness has to be larger to equalize the fluxes. Thus, it *appears* as if electrons have moved from tube 1 to tube 2 to follow the ions, but in actuality, electrons were "moved" only by a small adjustment of the sheath drops. As long as the electrons have a mechanism to follow the ions, keeping the plasma quasineutral, the Boltzmann relation will be followed even across **B**. The re-establishment of neutrality by sheath adjustment occurs in a nanosecond or so. Later, Fig. 8(a) is no longer valid. During the next tens of milliseconds, the discharge moves toward equilibrium and the sheath changes to that in Fig. 8(b). The difference in time scales means that the situation in Fig. 8(a) is so transitory that it is never seen. Electrons just seem to follow the ions across field lines with no problem.

Now that the electrons obey the Boltzmann relation, the plasma potential is high where the density is high. Thus, the sheath drop must be higher in tube 1 than in tube 2, as seen in Fig. 8(b). This creates a radial electric field **E** pointing inward (opposite to that in the transitory stage), driving the ions toward the center. Since **E** is scaled to T_e, the ions can move much faster than diffusion at temperature T_i. As the ions flow inward from an outside source, they will accumulate in the center if axial losses are small. The density gradient will flatten out and then reverse. This is the intermediate stage of approach to equilibrium. After reaching equilibrium, the density has to be flat or peaked on axis in order for the Boltzmann relation to generate the appropriate E-field to drive the ions outward toward the sidewall. The equilibrium situation can be represented by Fig. 8(b) if tubes 1 and 2 are interchanged, so that the higher-density tube is nearer the center. The density has to be peaked on axis because otherwise the ions will be driven inward and have nowhere to go. The ions cannot escape axially fast enough because E_z has to be small. This is a consequence of the Boltzmann relation when the scalelength of $n(z)$ is of the order of the plasma length. The cylinder, of course, cannot be very short and fat in this model. Note that the short-circuit effect cannot change T_e on different magnetic tubes, so T_e can vary radially. The Boltzmann relation is followed on each tube with the local T_e. This is taken fully into account in our computations for non-uniform $T_e(r)$.

The sheath conditions described above assume insulating endplates. If the endplates are conducting, electrons can cross field lines inside the conductor. However, this mechanism cannot inject electrons into tubes where more electrons are needed unless the endplates are hot enough to emit electrons. The only way to maintain quasineutrality is to adjust the sheath voltages. If this mechanism were not available, ions diffusing from high to low density would cause a space charge and an electric field that stops their diffusion. Thus, hollow density profiles can occur only in discharges long enough to prevent the short-circuit effect. Violation of normal ambipolar diffusion by the short-circuit effect has been detected by Kaganovich et al.[28] Non-Maxwellian electron distributions have been measured in low-density plasmas by Godyak et al.[29] These small deviations would have little effect on equilibrium profiles in denser plasmas. Theoretical

predictions of non-Maxwellian electrons have been expressed by Allen[30] and Zimmerman et al.,[31] but these concern current-carrying or flowing plasmas.

Sections VI and VII add realistic effects to the framework sketched above. Ionization balance determines a relationship between T_e and n_n. Neutral depletion determines how $n_n(r)$ varies with power. To avoid the rescaling of r to ρ, the EQM code solves the dimensional equation (16) with all quantities varying with r except T_e. Energy balance yields $T_e(r)$ but requires details on how rf power is applied. For that, we combine EQM with the HELIC code for helicon discharges. The result yields not only all radial profiles but also the absolute magnitudes of density and temperature.

VI. IONIZATION BALANCE

Equation (16) for the radial profiles allows n_n and T_e to vary with radius, but they cannot vary arbitrarily. In equilibrium, the number of ions leaving each radial shell must be exactly balanced by the number created there by ionization. Let $n_T(r)$ be the total number of ions in a shell of width dr at r. The input of ions into the shell per unit length (with $n_e = n_i = n$) is

$$\frac{dn_T(r)}{dt} = 2\pi r dr \cdot n(r) n_n(r) \cdot \langle \sigma v \rangle_{ion}(T_e). \tag{23}$$

The loss of ions from the shell is

$$-\frac{dn_T(r)}{dt} = 2\pi r dr \nabla \cdot [n(r)v(r)] = 2\pi r dr \cdot \frac{1}{r}\frac{d}{dr}[rn(r)v(r)]. \tag{24}$$

Equating these gives

$$\frac{1}{nr}\frac{d}{dr}(rnv) = n_n P_i(T_e), \tag{25}$$

where n and v are functions or r found from the solution of Eq. (16).

We can now calculate the relation between temperature T_e and pressure p_0 when n_n is uniform, with neutral depletion neglected. This is found by simultaneously solving Eqs. (16)

FIG. 10. (Color online) Relation between T_e and pressure in argon discharges of various radii. The relation between n_n and p_o is given by Eq. (29). The curves are in the same order as the legend.

and (25) requiring that the Bohm sheath condition $v = c_s$ be met at $r = a$. Let $a = 2.5$ cm and $p_0 = 10$ mTorr of argon. Solutions of Eqs. (16) and (25) together for various values of KT_e are shown in Fig. 9. It is seen that only one value of T_e gives $v = c_s$ at $r = 2.5$ cm when we use the dimensional Eq. (16). Repeating this for various pressures gives the $T_e - p_o$ relationship for argon, as shown in Fig. 10. Each radius a will have a different curve, since the surface-to-volume ratio varies as $1/a$. These are for uniform pressure and negligible end losses. The variation of T_e with r is negligibly small because of the sensitivity of P_i to T_e. Figure 10 is a great improvement over previous calculations of the $T_e - p_o$ curve because it is derived from *local* ionization balance with known density gradients instead of ionization balance averaged over the whole plasma, as in previous work.[32,33]

When the change of T_e with p_0 is taken into account, the profiles change as would be expected. This is shown in Fig. 11 for three pressures. The center-to-edge density ratio changes as normally predicted. At 100 mTorr, the curve resembles the usual Bessel function solution obtained from diffusion theory. At 3 mTorr, the curve resembles that for a collisionless plasma. The middle curve is the intermediate case which our equations can treat accurately.
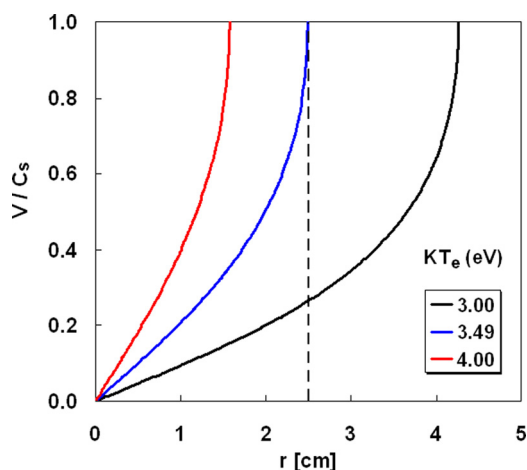

FIG. 9. (Color online) Profiles of $v(r)$ in a 2.5-cm radius, 10-mTorr argon discharge. Only one value of T_e gives the right position for the sheath edge.
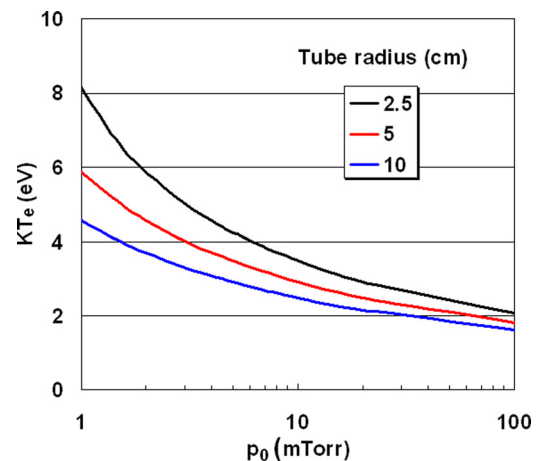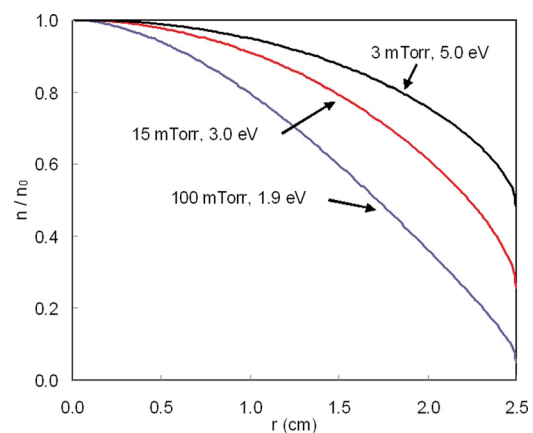

FIG. 11. (Color online) Density profiles at three pressures, computed with the corresponding KT_e given in Fig. 10 for $a = 2.5$ cm.

VII. NEUTRAL DEPLETION

To treat neutral depletion, we need to develop an equation for $n_n(r)$. Motion of the neutral gas can be treated with the diffusion equation if their mean free paths are short enough. The total collision cross section ν_{nn} between the neutral argon atoms is given by Phelps *et al.*[34] and varies only between 2 and 3×10^{-12} cm^2 for KT_n between 0.05 and 1.0 eV. This is the likely range of neutral energies before and after a charge-exchange collision. The corresponding mean free path varies from ~ 0.1 cm at 20 mTorr to ~ 1.5 cm at 1 mTorr. The use of the diffusion equation is, therefore, justified unless the discharge tube is very small.

Except for very narrow tubes, the neutral flux Γ is given by

$$\Gamma = n_n v_n = -D\nabla n_n, \tag{26}$$

where the diffusion coefficient D is defined by

$$D = KT_n/M\nu_{nn}. \tag{27}$$

Neutrals are lost by ionization and are replenished by injection of gas from outside the plasma. With Eq. (26), the equation of continuity for neutrals can be written as

$$\nabla \cdot \Gamma = -D\nabla^2 n_n - \nabla D \cdot \nabla n_n = -n_n n P_i, \tag{28}$$

where P_i is the ionization probability defined by Eq. (2). Equation (28) is to be solved subject to a boundary condition which is the source term for the neutrals.

Since the neutrals are injected at locations that differ from machine to machine, we have to make a reasonable model that will apply to all machines. Figure 12 illustrates the path of a typical neutral atom as it bounces against the tube walls and makes charge-exchange collisions with ions. We make the basic approximation that the input flux $\Gamma(a)$ is uniform in the azimuthal and axial directions regardless of the positions of the input tube and the pump line. This preserves the one-dimensional nature of the problem. Let p_0 be the pressure in mTorr at the inlet. This is related to the neutral density by

$$n_n = N_0 p_0, \quad N_0 = 3.3 \times 10^{13} \text{ cm}^{-3}. \tag{29}$$

This follows from the ideal gas law for monatomic gases at 20 C (293 K or 0.025 eV). The boundary condition is then

$$\Gamma(a) = n_n v_{th0} = N_0 p_0 (KT_n/2\pi M)^{1/2}. \tag{30}$$

Before the discharge is struck, there is a balance between the input and output of gas. The input is usually given in SCCM (standard cubic centimeters per minute), where 1 SCCM $= 4.17 \times 10^{17}$ s^{-1}. The pumping speed S is given in liters/s, usually limited by the conductance of a baffle. One l/s at a pressure p_0 is $10^3 N_0 p_0 = 3.3 \times 10^{16}$ atoms/s. The neutral pressure is, therefore, 12.7 SCCM/S mTorr. In the presence of plasma, however, the neutrals are heated and T_n may be different at the input and output. After a charge exchange collision, the neutral acquires an ion energy or order of 1 eV. After an ionization, the new ion has an energy above 0.025 eV and travels to the wall, where it is neutralized and reenters the plasma as a neutral. The mean free paths are short, so the neutrals are thermalized at a higher temperature. Since the degree of ionization is usually less than 1%, we shall neglect the difference in T_n between the input and output. The working hypothesis is that the fast neutrals and ions strike the wall and come back into the discharge as cool neutrals. These neutrals are distributed uniformly by collisions. The same flux leaves the boundary and enters the pump. Therefore, these processes do not change the overall input and output rates, so the boundary condition of Eq. (30) is still valid. Basically, the recycling of ions means that the plasma exists in a static neutral background replenished with a slow flow of gas in and out of the chamber. With neglect of variations in T_n, D is constant and Eq. (28) becomes

$$D\nabla^2 n_n = n_n n P_i, \tag{31}$$

which is to be solved with the boundary conditions (30) and $dn_n/dr = 0$ at $r = 0$.

The program EQM solves the three Eqs. (16), (25), and (31) simultaneously using a 4th order Runge-Kutta process to do the integrations. Examples of neutral depletion are shown in Figs. 13 and 14. If the plasma density is kept constant, Fig. 13 shows that neutral profiles are less affected at higher
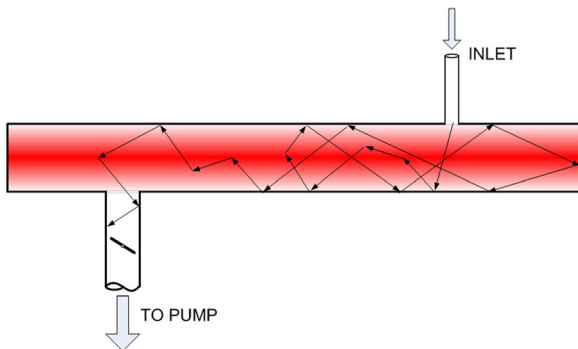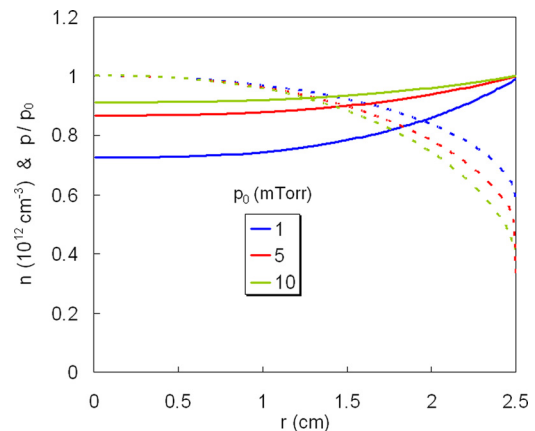
FIG. 12. (Color online) Typical path of a neutral atom in a plasma discharge. The positions of the inlet and outlet are arbitrary. The free paths have been lengthened for clarity. A baffle in the pump line is often used to limit the pumping speed at high pressures.

FIG. 13. (Color online) Neutral pressure profiles (solid lines) for argon discharges in a 5-cm diameter tube with initial pressures $p_0 = 1$, 5, and 10 mTorr at 400 K. The corresponding plasma density profiles peaked at 10^{12} cm^{-3} are shown by the dotted curves. 1 mTorr is the bottom line.

pressure. The plasma profiles change slightly because of the slower diffusion at higher pressure. Increasing the tube diameter to 10 cm has little effect on the relative profiles.

Figure 14 shows the dramatic effect of higher electron temperature at low pressure. With higher ionization fraction, less than half the neutrals reach the axis. The corresponding KT_e profiles show the inverse relation between T_e and n_n predicted by Eqs. (16) and (25). When n_n falls to the order of the electron density, as in the $n_0 = 5 \times 10^{12}$ cm^{-3} case, KT_e has to rise to extraordinary values (in theory) to provide the requisite ionization at such low pressures. These temperatures are, of course, unrealistic. Argon's inelastic threshold is around 12 eV, so that radiation losses limit KT_e to below 5 eV or so. The problem with these high T_e's is that we have not yet considered energy balance. To do so requires more detail about the energy gain and loss processes for a specific discharge. In Sec. VIII, we do this for helicon and ICP discharges which are treated by the HELIC program.[35]

Neutral depletion has been observed in experiment, for instance, by Yun et al.[36] and Aanesland et al.[37] Fruchtman et al.[38,39] have calculated neutral depletion in plane geometry invoking pressure balance with the plasma. They showed that radial transport is enhanced with lower n_n, and that non-monotonic density profiles can occur with axial diffusion, an effect neglected in this work.

VIII. HELICONS AND HELIC

In helicon discharges, the TG mode causes highly non-uniform ionization such that the power input $P(r)$ has a large peak near the edge of the plasma. This occurs because the TG mode deposits rf energy near the edge, raising T_e there, thus exponentially increasing the ionization rate at the edge. Nonetheless, measured density profiles are always peaked on axis. How this happens can be seen from Eq. (9), the Boltzmann relation. Initially, ionization produces a peak in density near $r = a$. With Boltzmann electrons, the potential ϕ has to follow the density, so it also peaks near $r = a$, resulting in an inward electric field. The ions are driven inward by $E(r)$, and the electrons follow them via the short-circuit effect. The density created near the boundary is pushed inwards by the electric field. This process can be followed in time-
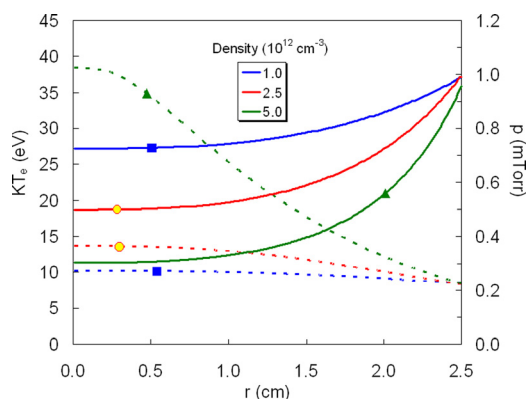
dependent calculations. In steady state, the only possible density profile is peaked at the center; a time-independent profile peaked at the edge is not possible if there is a short-circuit effect.

Many computer codes have been developed for the wave and absorption properties of helicon waves. Some are given here,[40–45] but these codes are not accessible for others to use. To calculate $T_e(r)$ produced by the non-uniform energy deposition in helicon discharges, we therefore use the HELIC code written by Arnush,[35] which has a user-friendly interface devised by one of us (F.C.). This will allow determinations of the absolute values of density and temperature to compare with experiments. The HELIC program was made for rapid experimental design. To achieve this, the equilibrium density n_0 and magnetic field $\mathbf{B}_0$ are assumed uniform along the axis z of a circular cylinder. However, n_0, KT_e, and pressure p_0 (but not $\mathbf{B}_0$) may vary with radius r in equilibrium. The plasma radius a and the antenna radius b are to be specified, as well as a ground-plane radius c, whose value is unimportant as long as it is large. The antenna can be any one of several popular types. The cylinder can be infinite in length or bounded by endplates that can be insulating or conducting. If it is bounded, the distance from the midplane of the antenna to one endplate and the total length between endplates can be specified. For a given gas, pressure, and rf frequency, HELIC then calculates the electric and magnetic fields, and the plasma current, of the coupled helicon-TG wave. More importantly, it integrates them to obtain the radial and axial energy deposition profiles and the total plasma resistance.

IX. ENERGY BALANCE

Once the inputs have been specified, HELIC calculates $P(r)$, which is the local power deposition at each radius, integrated over z. It also yields $P(z)$ integrated over radius, but we do not need this yet. The total rf power P_{in} absorbed by the plasma is, by definition,

$$P_{in} = \int_0^a P(r) r \, dr, \tag{32}$$

where $P(r) r \, dr$ is the power deposited into each cylindrical shell, with the 2π incorporated in $P(r)$. $P(r)$ is calculated by integration over the local power deposition $\mathbf{E}^* \cdot \mathbf{J}$, where $\mathbf{E}$ and $\mathbf{J}$ are the rf electric field and current of the helicon wave. P_{in} can also be calculated from the antenna loading. If I_0 is the peak antenna current and R is the load resistance that it "sees," P_{in} is also given by

$$P_{in} = \frac{1}{2} I_0^2 R. \tag{33}$$

R is the same as the plasma resistance R_p arising from electron collisions with ions and neutrals, including Landau damping. HELIC calculates R in ohms, and P_{in} and $P(r)$ are given for $I_0 = 1$ A.

Note, however, that P_{in} differs from the power P_{rf} from the power supply because of resistive losses R_c in the

FIG. 14. (Color online) Neutral pressure profiles in the same tube with $p_0 = 1$ mTorr and various peak plasma densities. The corresponding T_e profiles (dotted lines) are identified by the symbols.

circuitry. At low densities, a R_c of 0.5 Ω can be comparable to R_p. The relation is[46]

$$P_{in} = P_{rf} \frac{R_p}{R_p + R_c}. \tag{34}$$

First, let us calculate *overall* energy balance. The power lost from the plasma, P_{out}, consists of three terms: W_i, W_e, and W_r, where W_i and W_e are the kinetic energies carried out by ions and electrons leaving the plasma, and W_r is the (mostly radiative) loss by electrons making inelastic collisions. Each ion leaving the plasma carries out an energy consisting of $\frac{1}{2}KT_e$ of Bohm energy entering the sheath plus a sheath drop of about $5.4KT_e$ in argon,[33,47] so it carries out about $6KT_e$. W_i has two terms, the first due to flow to the sidewall and the second due to flow to the endplates,

$$W_i = \left[n(a)c_s(a)2\pi aL + 2\int_0^a n(r)c_s(r)2\pi rdr \right] 6KT_e. \tag{35}$$

Here, we had to choose a length L of the plasma. If the plasma is nonuniform axially, L can be estimated from the power deposition profile $P(z)$ mentioned above. This can give an equivalent length if the plasma density varies in z.

Electrons leave mostly via the endplates, but the total flux has to equal the ion flux. Each electron carries out an energy[33,48] of about $2KT_e \approx W_i/3$. Thus, the conductive losses in watts are

$$W_i + W_e \approx (4/3)eW_i \quad W, \tag{36}$$

where Roman "e" is the electron charge in coulombs.

The inelastic loss W_r can be found from the E_c curve calculated by Vahedi.[49] E_c is the amount of energy expended by an average electron in making an ionization, taking into account the radiative losses in all the inelastic collisions made before the ionization. This depends on the temperature. The Vahedi curve (Fig. 15) can be fitted by the function

$$E_c(\text{eV}) = 23\exp(3.68/T_{eV}^{1.61}), \tag{37}$$

where T_{eV} is T_e in eV. The loss dW_r from each shell of unit length at radius r is then E_c times the local ionization rate,

$$dW_r = 2\pi rdr n_n(r)n(r)\langle\sigma v\rangle_{ion}E_c. \tag{38}$$
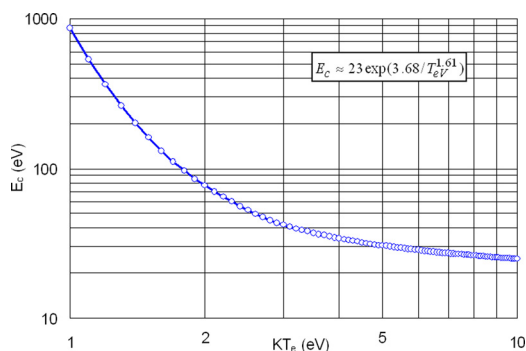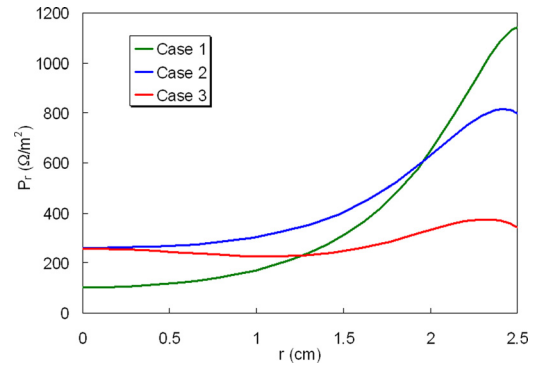
Defining

FIG. 16. (Color online) Radial energy deposition profiles for three cases computed by HELIC with different magnitudes of the TG mode. The densities are 12.6, 5.0, and 1.6×10^{11} cm^{-3} for cases 1-3. In all cases, B is 65G and tube radius is 2.5 cm.

$$F(T_e) \equiv E_c(T_e)\langle\sigma v\rangle_{ion}(T_e), \tag{39}$$

we write this as

$$dW_r = 2\pi rdr n_n(r)n(r)F[T_e(r)]. \tag{40}$$

Once $n(r)$, $n_n(r)$, and $T_e(r)$ have been determined by the EQM program, the total W_r in watts can be calculated by integration,

$$W_r = eL\int_0^a n_n(r)n(r)F[T_e(r)]2\pi rdr \quad W, \tag{41}$$

where Roman "e" is again the electron charge in coulombs. The total P_{out} is then

$$P_{out} = W_i + W_e + W_r, \tag{42}$$

which can be equated to P_{in} from Eq. (33) to yield the absolute value of plasma density $n(r)$ for any given value of antenna current I_0.

To evaluate *local* energy balance, we simplify the problem by neglecting the conductive losses, which are small compared with W_r for temperatures below ~4 eV. The input of energy to each cylindrical shell is given by the integrand of Eq. (32). The loss of energy to each shell is given by the integrand of Eq. (41) (including eL). Equating local P_{in} to local P_{out} determines the temperature profile $T_e(r)$. That is,

FIG. 15. (Color online) Energy required to make one ionization vs. electron temperature.
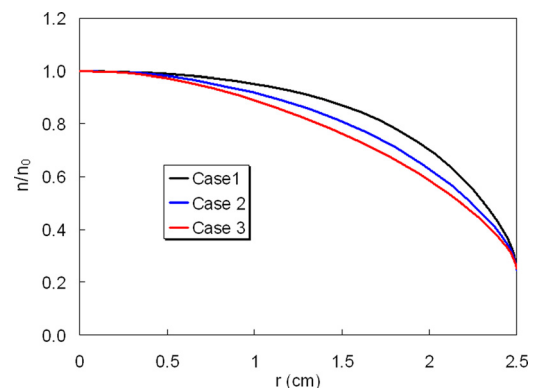

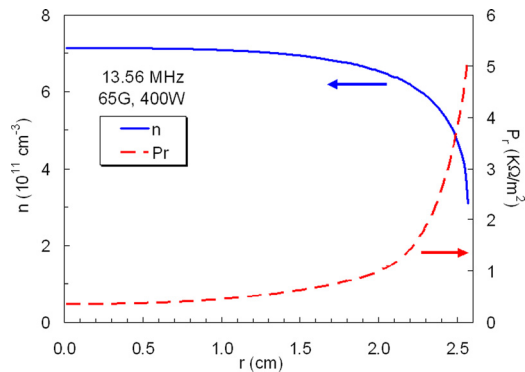FIG. 17. (Color online) Density profiles computed by EQM for the $P(r)$ profiles of Fig. 16.

FIG. 18. (Color online) Curves of $n(r)$ (——) and $P_r(r)$ (- - -), obtained by iteration of EQM with HELIC, for a 15-mTorr helicon discharge at 65G with 400 W of rf at 13.56 MHz and $m = 0$ antenna.

FIG. 20. (Color online) Curves of $n(r)$ (——) and $P_r(r)$ (- - -), obtained by iteration of EQM with HELIC, for a 15-mTorr helicon discharge at 120G with 1000 W of rf at 27.12 MHz and $m = 0$ antenna.

when the input $P(r)$ is high, there will be more ionization there. This requires a high loss rate, which is accomplished by an increased T_e and, hence, a larger $F(T_e)$ in Eq. (41). A nonuniform deposition of rf energy giving a nonuniform ionization profile is expressed via the electron temperature profile.

X. ITERATIONS OF EQM WITH HELIC

The density, temperature, and neutral density profiles resulting from the highly nonuniform rf energy deposition of the combined helicon and TG waves can now be computed by iterating between the EQM and HELIC codes. Initially, EQM is solved with uniform ionization, giving $n(r)$, T_e, and $n_n(r)$. These profiles are fitted with a 6-degree polynomial to be entered into HELIC to obtain $P(r)$. Energy balance yields $T_e(r)$. This profile, representing nonuniform ionization, is then entered into EQM to obtain new profiles of n, T_e, and n_n. The process is repeated until it converges. It normally takes only five or six iterations for convergence.

Before showing iterations, we first show that edge-peaked energy deposition profiles produce density profiles that are peaked at the center rather than at the edge. Figure 16 shows three $P(r)$ curves produced by HELIC under different conditions. One is highly peaked at the edge; the second is less peaked; and the third has almost equal contributions from the TG and H modes. The density profiles produced
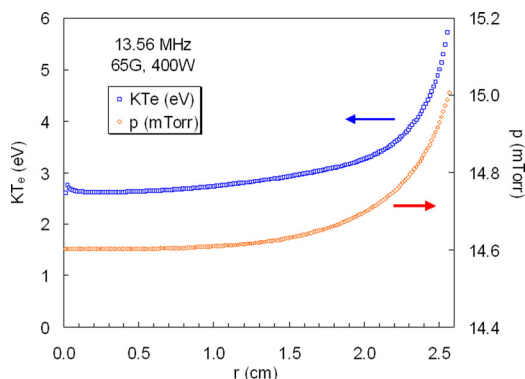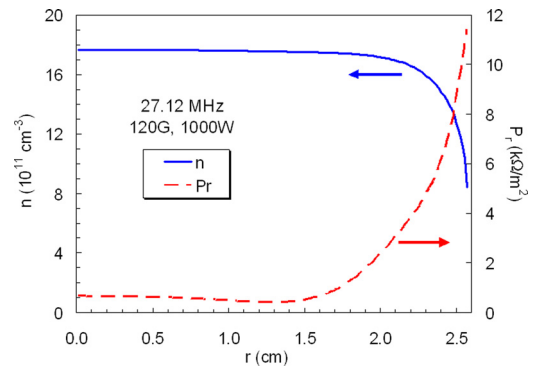
by EQM in these three cases are shown in Fig. 17. Case 1 has more density at large radii, but in all cases, the density is peaked on axis. This shows that hollow profiles are never produced when there is a short-circuit effect. The $P(r)$ profiles here are not yet consistent with the $n(r)$ profiles, because the $P(r)$ profiles were computed without knowing the exact $n(r)$.

We next show results in which the $P(r)$ profiles from HELIC are completely consistent with the $n(r)$ profiles from EQM, as obtained by iteration between the two programs. Two cases representing low and high powers for $m = 0$ loop antenna are shown in Figs. 18–21. With large TG-mode deposition at the edge, both cases have high T_e and, hence, high ionization at the edge, giving rise to the flat density profiles at the center. The 120-G, 1 kW, 27.12 MHz case in Fig. 20 has larger TG deposition at the edge, giving a flatter density profile. The higher density in that case also leads to higher neutral depletion: 0.8 mTorr compared with 0.4 mTorr in the lower power case. Note that the dip in $P(r)$ in Fig. 20 is reflected in the $T_e(r)$ profile in Fig. 21.

In Figs. 22 and 23, we show a larger plasma 10 cm rather than 5 cm in diameter, the pressure is lower at 5 mTorr, and the B-field is higher. Neutral depletion is higher because of the lower pressure. At the center of Fig. 23, T_e varies inversely with the pressure according to ionization balance, but near the edge T_e rises from the Trivelpiece-Gould heating there. These two regions are better separated with the larger
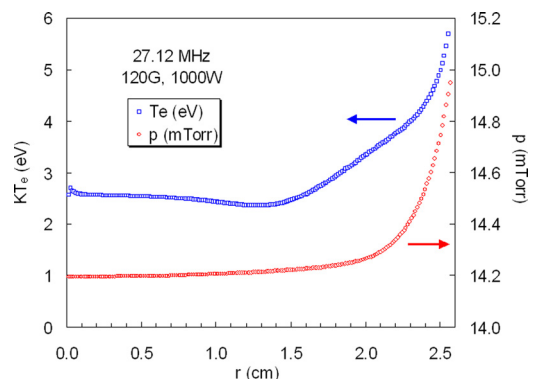

FIG. 19. (Color online) Radial profiles of KT_e and neutral pressure p corresponding to the discharge in Fig. 18. Note that p (right scale) has a suppressed zero.

FIG. 21. (Color online) Radial profiles of KT_e and neutral pressure p corresponding to the discharge in Fig. 20. Note that p (right scale) has a suppressed zero.
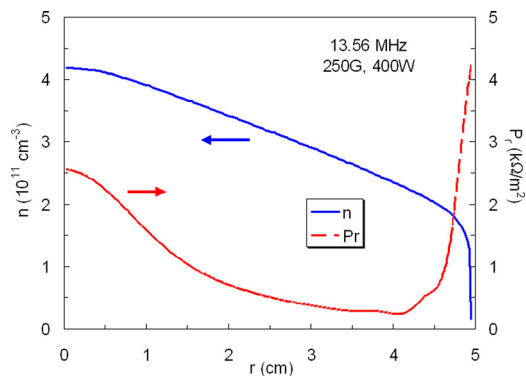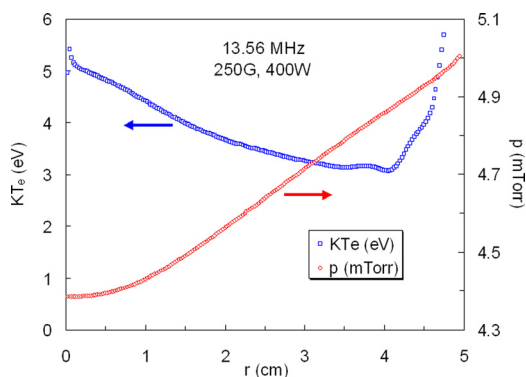
FIG. 22. (Color online) Curves of $n(r)$ (—) and $P_r(r)$ (- - -), obtained by iteration of EQM with HELIC, for a larger 5-mTorr helicon discharge at 250 G with 400 W of rf at 13.56 MHz and $m = 0$ antenna.
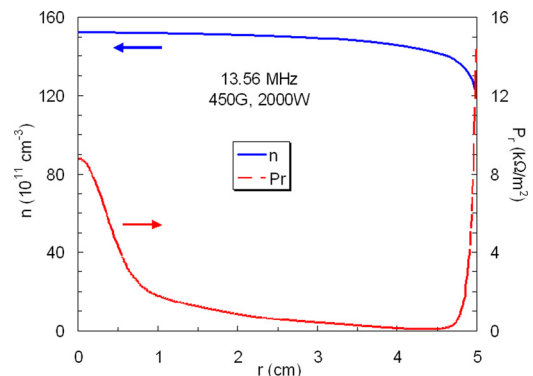

FIG. 24. (Color online) Curves of $n(r)$ (—) and $P_r(r)$ (- - -), obtained by iteration of EQM with HELIC, for a larger 3-mTorr helicon discharge at 450 G with 2000 W of rf at 13.56 MHz and a half-wavelength $m = 1$ helical antenna.

diameter. Note that the short-circuit effect cannot transport electron *temperature* across **B**; the heat conductivity is still reduced by the magnetic field. In Fig. 22, we see that the antenna produces much higher absorption on axis, and this results in a "triangular" density profile. The triangularity occurs so often that it inspired one of us[50] to conjecture that it is caused by nonlinear diffusion in combination with the short-circuit effect and a deposition profile like that in Fig. 22. This conjecture is now confirmed in the present calculations, which include all nonlinearities.

If we now change to a helical antenna, $m = 1$ left-hand helix (which generates a right-hand helical wave), and apply higher magnetic field and rf power, we obtain the curves in Figs. 24 and 25. Neutral depletion is high because of the low pressure and very high density. In Fig. 24, we see that the helical antenna produces a narrower absorption peak on axis than in Fig. 22, and this results in a flatter density profile. This result was not expected. Note that T_e no longer reaches the unreasonable values in Fig. 14, now that energy balance has been imposed.

This high-power case was the original motivation for this work because of the occurrence of the Big Blue Mode (BBM). Boswell[51] first observed this mode, in which the plasma collapsed at high power to a narrow bright central column with density approaching 10^{14} cm^{-3}. It was photographed by Blackwell.[52] We believe this to be an extreme

case of neutral depletion, in which the neutral density almost vanishes near the axis, requiring T_e to rise to a very high value to maintain ionization balance. There would be an *ionization instability,* and the plasma would have to contract to be consistent with the available rf power. At those temperatures, argon would be multiply ionized. Although an EQM-HELIC iteration should be able to predict the BBM, a Vahedi-type curve does not yet exist for the radiative losses, and the BBM is still an unfinished problem.

XI. COMPARISON WITH EXPERIMENTS

Figure 26 shows density profiles obtainable with the ICP of Fig. 1. These resemble the centrally peaked profiles in Fig. 17 for energy deposition at the edge. Such results motivated studies of anomalous skin effect,[53,54] but we have shown here that simple equilibrium theory can account for most of the effect.

For smaller intense discharges, there are very few results reported for measurements in the antenna region because of the intense rf environment and high density there. Measurements in the ejected plasma outside the discharge tube do not relate directly to the predictions of our theory and computational programs. However, a linear system was no longer available. The examples given in Figs. 18–21 are computed for the discharge tube shown in Fig. 27 in a system designed
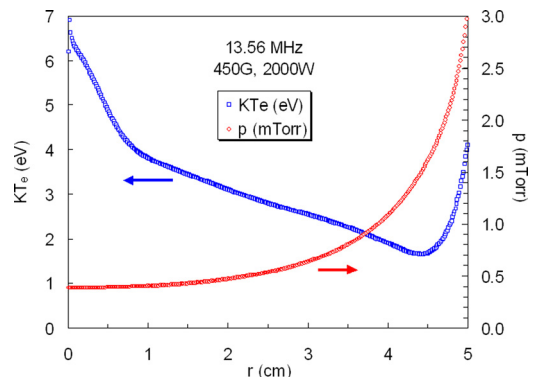

FIG. 23. (Color online) Radial profiles of KT_e and neutral pressure p corresponding to the discharge in Fig. 22. Note that p (right scale) has a suppressed zero.

FIG. 25. (Color online) Radial profiles of KT_e and neutral pressure p corresponding to the discharge in Fig. 24. Note that p (right scale) has a suppressed zero.
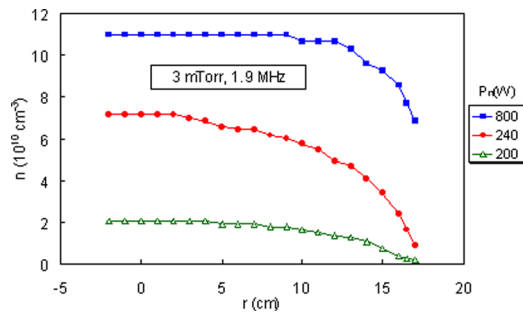
FIG. 26. (Color online) Radial profiles of plasma density in the machine in Fig. 1 at various rf powers. Data were taken by J. D. Evans in our laboratory in 1998 under contract with PlasmaTherm.

with a probe inside the discharge. The magnetic field was from a permanent magnet above the tube, as shown in Fig. 28, and could be varied by vertical separation. The plasma is ejected from the tube downwards into an experimental chamber. The B-field diverges and is non-uniform there, but it is quite uniform within the tube. Although it is far from a uniform cylinder, this device can provide qualitative checks of our theory. HELIC is configured for this geometry by setting the distance between endplates in HELIC to a large number (200 cm), and placing the antenna within 4 cm of one endplate. The fact that the magnetic field shape here is not the uniform one assumed in HELIC does not greatly affect the results because almost all the wave action and ionization are within the uniform-field region inside tube, where our theory applies. Only a few measurements below the discharge will be shown here. A complete paper on the experiment will be written later.

It was not possible to measure radial profiles inside the discharge tube, but $n(r)$ could be measured with a horizontal probe in the main chamber 6.8 cm below the tube. This is shown in Fig. 29 for a magnet position that produces ~65G at the antenna. Magnetic divergence and diffusion have spread $n(r)$, but the central peaking as predicted by our theory is seen. KT_e, however, has edge peaks due to the TG mode. The plasma potential V_s was calculated from the slope of $\ln(I_e)$ using $n(r)$ from saturation ion current. To check that the Boltzmann relation is obeyed, we can compare $V_s(r)$ with that calculated from $n(r)$ using Eq. (9) with the local T_e. This
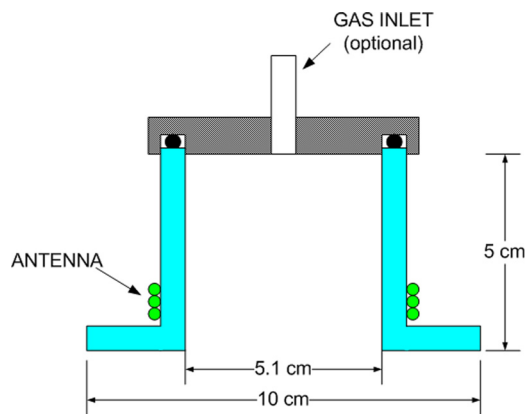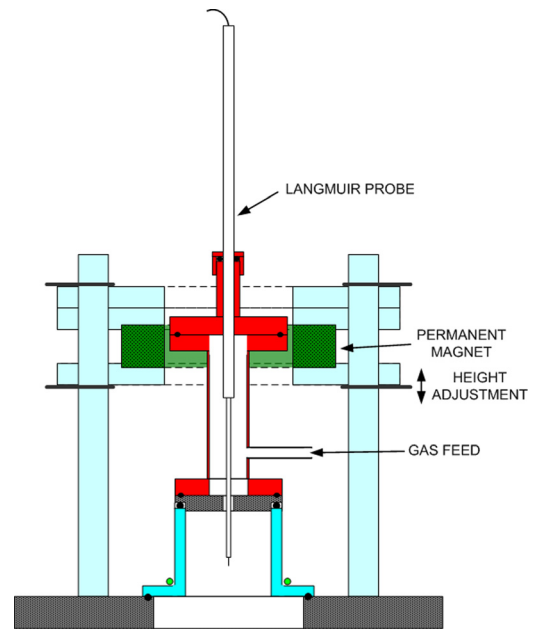

FIG. 28. (Color online) Experimental setup with NdFeB permanent magnet and rf-compensated Langmuir probe. The magnetic field can be adjusted by moving the magnet vertically. Two magnets can be used to double the field. The plasma is ejected into a large chamber below. Inside the discharge, the magnetic field lines are vertical with a slight divergence.

is shown by the solid line V_s(Maxw) in Fig. 29, which is somewhat flatter than the measured $V_s(r)$ but has the right magnitude. Figure 30 shows data with two magnets placed closer to the discharge, so that the B-field is both much higher and more divergent. $B(z)$ varies from 200 to 360G inside the discharge. At this large field, the TG mode is strongly localized to the edge, and $n(r)$ no longer peaks at the center. Our discharge is quite short, and it is possible for ions to be driven inwards by a reverse E-field and to escape out the ends. Thus, our 1-D theory does not hold in this case.

Since the HELIC code yields the exact power in watts deposited in the plasma for a given power in the antenna, and the Vahedi curve gives the power lost in radiation, it is possible to calculate the absolute value of the density in the discharge tube for given rf power and pressure. Order-of-
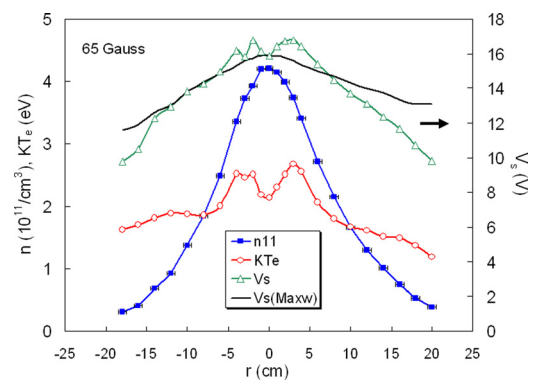

FIG. 27. (Color online) Diagram of the quartz discharge tube with aluminum top plate. The antenna shown is for 13.56 MHz.

FIG. 29. (Color online) Radial profiles of density (■), KT_e (O), plasma potential (△), and Boltzmann potential (—) measured 6.8 cm downstream from the source at 15 mTorr with 400 W of rf at 27.12 MHz and a B-field of ~65 G. The error bars show the length of the 12.7 μm diameter probe tip. Relative density is good to 3%, but absolute density only to ±10% in probe area.
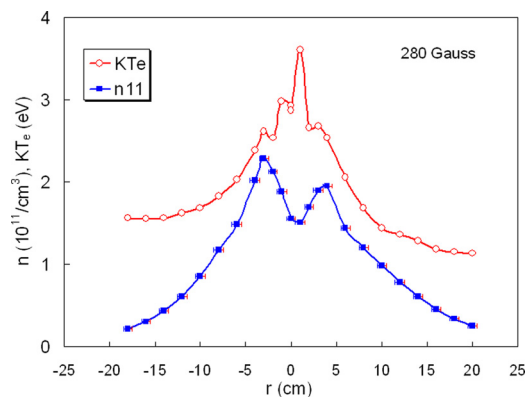
FIG. 30. (Color online) Data similar to those in Fig. 29 but with a double magnet set to produce 280 G at the antenna.

FIG. 32. (Color online) Absolute agreement of plasma density between theory and experiment for various values of discharge length L consistent with the axial deposition profile $P(z)$, shown in Fig. 31.

magnitude agreement would give credibility to the calculations. There is a fundamental uncertainty in that the discharge does not have an exact length, as in the theory. However, HELIC also calculates $P(z)$, the distribution of power deposition along the axis, and from this, we can estimate the effective length of the discharge, as shown in Fig. 31. Figure 32 shows the absolute values of density on axis as calculated with EQM-HELIC iteration and as measured. The range of possible effective lengths is also shown.

XII. SUMMARY

A computational program EQM was devised to calculate equilibrium profiles of density, ion drift velocity, electron temperature, and neutral depletion in cylindrical discharges. The major restrictions are that the electrons are Maxwellian and that only radial gradients are important. If the Simon short-circuit effect at the endplates is effective, the Boltzmann relation can be followed even if there is a strong magnetic field. Under such conditions, we find, surprisingly, that the solutions are self-similar, and the profiles follow a semi-universal law independent of pressure and discharge diameter. The density profiles always peak on axis, even if the ionization is at the edge. Furthermore, the radial ion velocity reaches the acoustic speed at a radius which can be defined as the sheath edge. In this "plasma solution," all ionization and collision effects are accounted for in detail, so that there

is no need to assume a pre-sheath. Implementing ionization balance at each radius gives the inverse relation between neutral pressure and electron temperature accurately without arbitrary averaging.

Accounting for energy balance in rf discharges requires additional information on antenna coupling. For helicon sources, this is provided by the HELIC program. By iterating EQM with HELIC to get consistent profiles, the density and other profiles can be calculated for a variety of conditions such as tube size, rf frequency, and magnetic field. The method is powerful enough to yield absolute values of the density for given rf input. Examples of such iterations are given. "Hollow" density profiles do not occur in this steady-state theory, and we have only recently observed them. They have been seen in experiments by others. In those cases, either the discharge was pulsed or other conditions prevented the short-circuit effect from being operative.
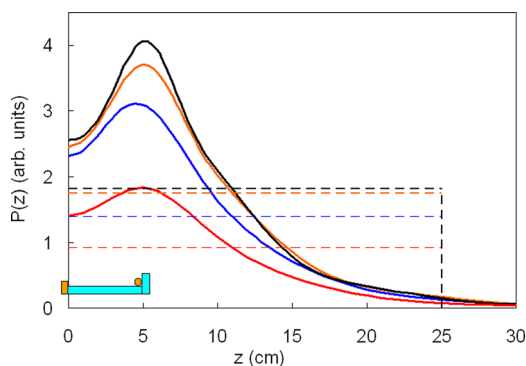
FIG. 31. (Color online) Axial deposition profiles $P(z)$ for the four points computed for $L = 25$ cm in Fig. 32. The rectangles have the same area as that under the corresponding curve. The inset shows the position of the discharge tube and antenna.
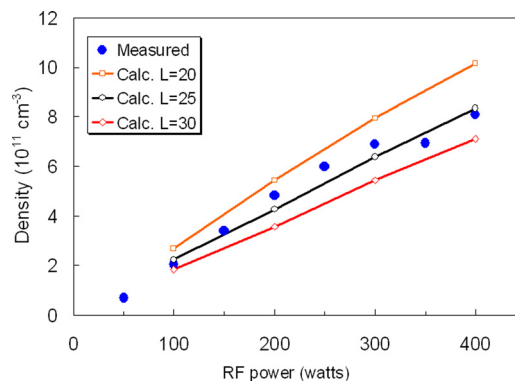
APPENDIX: CROSS SECTIONS

1. Argon ionization cross section

The cross section for ionization of argon by electrons is well known. We have fitted the ionization probability $\langle \sigma v \rangle$ as a function of KT_e with the following formula:

$$\langle \sigma v \rangle_{\mathrm{ion}} = \exp\left[-15.8 - \left(17.7 / T_{eV}^{0.91}\right)\right] \mathrm{cm}^3/\mathrm{s}.$$

2. Argon charge exchange cross section

A critical cross section in our diffusion calculations is the Ar^+-Ar resonant charge exchange cross section. Since it is difficult to produce monoenergetic beams at energies of the order of 1 eV, the first data were from measurements of

mobility, from which the cross section could be calculated. For instance, Biondi and Chanin[55] published this in 1954. These data were smoothed and summarized by Brown[56] and later improved by Sheldon.[57] The following papers give direct measurements of this cross section.[58–62] In this paper, we used the data of Rapp and Francis,[57] which agree with those of Sheldon at 1 and 10 eV. There was no agreement among the others.

The cross section can be parametrized by

$$\sigma_{cx}(\text{cm}^2) = 6.3 \times 10^{-14}(\text{A}/E_i)^{0.14}\Phi_{ioniz}^{-1.07},$$

where A is 40 and the ionization threshold Φ_{ioniz} is 15.76 eV for argon. E_i is the ion energy in eV, approximately equal to KT_i.

3. Argon neutral-neutral cross section

To calculate neutral depletion, we needed the collisional cross section between argon neutral atoms. There is fortunately recent, accurate data on this by Phelps et al.[63] It is explained in the paper that σ_t, rather than σ_v, is the proper cross section to use, and this does not vary much over the energy range of interest.

[1]J. J. Thomson, *Conduction of Electricity through Gases* (Cambridge University Press, Cambridge, England, 1903).
[2]I. Langmuir, Phys. Rev. **33**, 954 (1929).
[3]S. Chapman and T. G. Cowling, *The Mathematical Theory of Non-uniform Gases* (Cambridge University Press, Cambridge, UK, 1960).
[4]L. M. Biberman, V. S. Vorob'ev, and I. T. Yakubov, *Kinetics of Nonequilibrium Low-temperature Plasmas* (Consultants Bureau, New York, 1987).
[5]J.-L. Delcroix, *Introduction to the Theory of Ionized Gases* (Interscience, New York, 1960).
[6]J. L. Delcroix, *Physique des Plasmas,* Tome 2: *Gaz faiblement ionises* (Dunod, Paris, 1966).
[7]R. N. Franklin, *Plasma Phenomena in Gas Discharges* (Clarendon, Oxford, UK, 1976).
[8]E. R. Harrison and W. B. Thompson, Proc. Phys. Soc. **74**, 145 (1959).
[9]F. F. Chen, Nuovo Cimento **26**, 698 (1962).
[10]D. Bohm, *Characteristics of Electrical Discharges in Magnetic Fields*, edited by A. Guthry and R. K. Wakerling (McGraw-Hill, New York, 1949).
[11]F. F. Chen, *Introduction to Plasma Physics and Controlled Fusion*, 2nd ed. (Plenum, New York, 1984), Vol. 1.
[12]K.-U. Riemann, Phys. Plasmas **4**, 4158 (1997).
[13]M. A. Lieberman and A. J. Lichtenberg, *Principles of Plasma Discharges and Materials Processing*, 2nd ed. (Wiley, Hoboken, NJ, 2005).
[14]F. F. Chen and J. P. Chang, *Principles of Plasma Processing* (Kluwer/Plenum, New York, 2002).
[15]A. W. Trivelpiece and R. W. Gould, J. Appl. Phys. **30**, 1784 (1959).
[16]B. Lorenz, M. Krämer, V. L. Selenin, and Y. M. Aliev, Plasma Sources Sci. Technol. **14**, 623 (2005).
[17]R. W. Boswell, Phys. Lett. A **33**, 457 (1970).
[18]V. A. Godyak, *Soviet Radio Frequency Discharge Research* (Delphic Associates, Falls Church, VA, 1986).
[19]M. A. Lieberman and A. J. Lichtenberg, *Principles of Plasma Discharges and Materials Processing*, 2nd ed. (Wiley, Hoboken, NJ, 2005), Sec. 5.3.
[20]N. Sternberg, V. Godyak, and D. Hoffman, Phys. Plasmas **13**, 063511 (2006).
[21]A. Fruchtman, G. Makrinich, and J. Ashkenazy, Plasma Sources Sci. Technol. **14**, 152 (2005).
[22]A. Fruchtman, Plasma Sources Sci. Technol. **18**, 025033 (2009).
[23]F. F. Chen, *Introduction to Plasma Physics and Controlled Fusion*, 2nd ed. (Plenum, New York, 1984), Vol. 1, p. 239.
[24]F. F. Chen, *Introduction to Plasma Physics and Controlled Fusion*, 2nd ed. (Plenum, New York, 1984), Vol. 1, p. 58ff.
[25]F. F. Chen, *Introduction to Plasma Physics and Controlled Fusion*, 2nd ed. (Plenum, New York, 1984), Vol. 1, p. 173.
[26]A. Simon, Phys. Rev. **98**, 317 (1955).
[27]V. A. Godyak, *Soviet Radio Frequency Discharge Research* (Delphic Associates, Falls Church, VA, 1986).
[28]D. Kaganovich, V. A. Rozhansky, L. D. Tsendin, and I. Y. Veselova, Plasma Sources Sci. Technol. **5**, 743 (1996).
[29]V. A. Godyak, R. B. Piejak, and B. M. Alexandrovich, Plasma Sources Sci. Technol. **11**, 525 (2002).
[30]J. E. Allen, Contrib. Plasma Phys. **48**(5-7), 1 (2008).
[31]T. M. G. Zimmermann, M. Coppins, and J. E. Allen, Phys. Plasmas **17**, 022301 (2010).
[32]M. A. Lieberman and A. J. Lichtenberg, *Principles of Plasma Discharges and Materials Processing*, 2nd ed. (Wiley, Hoboken, NJ, 2005), p. 334.
[33]F. F. Chen and J. P. Chang, *Principles of Plasma Processing* (Kluwer/Plenum, New York, 2002), pp. 70-71.
[34]A. V. Phelps et al., J. Phys. B **33**, 2965 (2000).
[35]D. Arnush, Phys. Plasmas **7**, 3042 (2000).
[36]S. Yun, K. Taylor, and G. R. Tynan, Phys. Plasmas **7**, 3448 (2000).
[37]A. Aanesland, L. Liard, G. Leray, J. Jolly, and P. Chabert, Appl. Phys. Lett. **91**, 121502 (2007).
[38]A. Fruchtman, G. Makrinich, P. Chabert, and J. M. Rax, Phys. Rev. Lett. **95**, 115002 (2005).
[39]A. Fruchtman, Phys. Plasmas **17**, 023502 (2010).
[40]K. P. Shamrai and V. B. Taranov, Plasma Sources Sci. Technol. **5**, 474 (1996).
[41]S. Cho, Phys. Plasmas **3**, 4268 (1996).
[42]I. V. Kamenski and G. G. Borg, Comput. Phys. Commun. **113**, 10 (1998).
[43]Y. Mouzouris and J. E. Scharer, Phys. Plasmas **5**, 4253 (1998).
[44]D. Bose, T. R. Govindan, and M. Mayyappan, IEEE Trans. Plasma Sci. **31**(4), 464 (2003).
[45]S. Cho and M. A. Lieberman, Phys. Plasmas **10**, 882 (2003).
[46]F. F. Chen and H. Torreblanca, Plasma Sources Sci. Technol. **16**, 593 (2007).
[47]M. A. Lieberman and A. J. Lichtenberg, *Principles of Plasma Discharges and Materials Processing*, 2nd ed. (Wiley, Hoboken, NJ, 2005), p. 333.
[48]M. A. Lieberman and A. J. Lichtenberg, *Principles of Plasma Discharges and Materials Processing*, 2nd ed. (Wiley, Hoboken, NJ, 2005), p. 37.
[49]V. Vahedi, "Modeling and simulation of rf discharges used for plasma processing," Ph.D. thesis, University of California, Berkeley, 1993. Recent data are from P. Vitello, LLNL.
[50]F. F. Chen, Plasma Sources Sci. Technol. **7**, 458 (1998).
[51]R. W. Boswell, private communication (1985).
[52]D. D. Blackwell and F. F. Chen, Plasma Sources Sci. Technol. **6**, 569 (1997).
[53]J. D. Evans and F. F. Chen, Phys. Rev. Lett. **86**, 5502 (2001).
[54]F. F. Chen, IEEE Trans. Plasma Sci. **34**, 718 (2006).
[55]M. A. Biondi and L. M. Chanin, Phys. Rev. **94**, 910 (1954).
[56]S. C. Brown, *Basic Data of Plasma Physics*, 2nd ed. (AIP, College Park, MD, 1994).
[57]J. W. Sheldon, Phys. Rev. Lett. **8**, 64 (1962).
[58]D. Rapp and W. E. Francis, J. Chem. Phys. **37**, 2631 (1962).
[59]B. J. Nichols and F. C. Witteborn, NASA Report TN D-3265 (Ames Research Center, 1966).
[60]M. I. Chibisov, JETP Lett. **24**, 46 (1976).
[61]H. R. Kaufman and R. S. Robinson, "Charge and momentum exchange in an ion beam," Technical Note KRI-03 (Kaufman and Robinson, Inc., 2003); R. S. Robinson, J. Vac. Sci. Technol. **16**(2), 185 (1979).
[62]S. A. Maiorov, O. F. Petrov, and V. E. Fortov, "Calculation of resonant charge exchange cross sections of ions of rubidium, cesium, mercury, and noble gases," in *Proceedings of the 34th EPS Conference on Plasma Physics, Warsaw, July 2007* (xx, xx, 2007), ECA Vol. 31F, P-2.115.
[63]A. V. Phelps, C. H. Greene, and J. P. Burke, Jr., J. Phys. B **33**, 2965 (2000).